

High harmonic spectra computed using time-dependent Kohn-Sham theory with Gaussian orbitals and a complex absorbing potential

Ying Zhu and John M. Herbert*

*Department of Chemistry & Biochemistry, and Chemical Physics Graduate Program,
The Ohio State University, Columbus, OH 43210*

(Dated: November 25, 2021)

High harmonic spectra for H_2 are simulated by solving the time-dependent Kohn-Sham equation in the presence of a strong laser field, using an atom-centered Gaussian representation of the orbitals and a complex absorbing potential to mitigate artifacts associated with the finite extent of the basis functions, such as spurious reflection of the outgoing electronic wave packet. Interference between the outgoing and reflected waves manifests in the Fourier transform of the time-dependent dipole moment function and leads to peak broadening in the high harmonic spectrum as well as the appearance of spurious peaks at energies well above the cutoff energy at which the harmonic progression is expected terminate. We demonstrate that well-resolved spectra can be obtained through the use of an atom-centered absorbing potential. As compared to grid-based algorithms for solving the time-dependent Kohn-Sham equations, the present approach is more readily extendible to larger polyatomic molecules.

I. INTRODUCTION

Experimental study of molecules and materials under short, intense femtosecond and even attosecond laser pulses is becoming possible due to the advent of ultra-short pulse technology based on high harmonic generation (HHG).¹⁻⁴ This has enabled the development of soft x-ray and extreme ultraviolet laser pulses with ultra-fast time resolution,⁵⁻⁷ even in tabletop instruments,⁸⁻¹⁰ which promises to make this technology more widely available in the near future. The strong-field phenomena that can be probed with this new generation of instruments poses challenges to well-developed theoretical models that work in the perturbative (weak-field) regime, as new phenomena arise in strong electric fields. These include above-threshold ionization, nonsequential ionization, multiphoton ionization, delayed photoemission, and HHG.¹¹⁻¹³ Attosecond experiments are expected to provide fundamental probes of electron correlation and ultrafast charge migration in both molecules and materials.¹³⁻¹⁶ Theoretical description of this emergent physics promises to push the envelope of computational quantum chemistry.¹⁷

In the context of time-dependent density functional theory (TDDFT),^{18,19} strong-field phenomena cannot be described within the linear-response approximation²⁰ that has become essentially synonymous (in quantum chemistry, at least) with the moniker of TDDFT.²¹ In principle, an exact theory can still be formulated even in the strong-field or non-perturbative regime, based on direct solution of the time-dependent Kohn-Sham equation.^{12,22} This approach is often called “real-time” TDDFT,²³ although we prefer the term *time-dependent Kohn-Sham* (TDKS) theory.^{24,25} In practice, however, there are significant questions as to whether existing

exchange-correlation functionals that invoke the adiabatic approximation are up to the task,^{12,23} although improving the description of the derivative discontinuity improves the description of ionization, even within the adiabatic approximation.²⁶

In the present work, we examine the HHG phenomenon in a simple test case, H_2 molecule, using an atom-centered Gaussian representation of the Kohn-Sham orbitals. Previous TDKS simulations of HHG in H_2 have emphasized the importance of using an exchange-correlation functional with correct asymptotic behavior.²⁷⁻³⁰ In some calculations, this has been achieved in practice by using either time-dependent Hartree-Fock (TDHF) theory or else the closely-related time-dependent configuration interaction singles (TD-CIS) method.^{29,31-33} Functionals with an explicit self-interaction correction have also been employed,^{27,28} as this helps with the aforementioned derivative discontinuity. Recently, the use of range-separated, “long-range corrected” (LRC) hybrid functionals³⁴⁻³⁹ has been considered for simulation of HHG in H_2 and other small molecules.³³ As compared to either generalized gradient approximations or even global hybrid functionals, LRC functionals do a much better job of approximating the derivative discontinuity.⁴⁰ The simulations presented herein will be based upon the LRC- ω PBE functional,³⁷ which was also used to simulate HHG in Ref. 33.

Rather than using a grid-based algorithm to solve the TDKS equations,^{22,27,28} we follow the path established by Saalfrank, Luppi, and others,^{29-33,41} using atom-centered Gaussian basis sets to represent the density. This makes TDKS simulations accessible with widely-available, general purpose quantum chemistry codes, and the compactness of the Gaussian representation offers the possibility to extend TDKS calculations to larger molecules than are feasible in grid-based representations. Even for H_2 , where both approaches are feasible, the Gaussian representation is found to be at least an order of magnitude more efficient,³⁰ and only that approach

*herbert@chemistry.ohio-state.edu

is scalable. This efficiency might be used, for example, to simulate HHG in a liquid or in a bulk crystal, both of which have been realized experimentally.^{7,42,43} For HHG in liquids, the role of molecular disorder has been emphasized,⁴⁴ suggesting that model systems larger than a single molecule are required to understand this phenomenon.

That said, previous work on small-molecule HHG has emphasized the important role that is played by Rydberg and continuum states,^{32,41,45} which is unsurprising given the role of tunneling ionization in the HHG process,^{1,2,16,46} yet these states are not well described by standard Gaussian basis sets and very diffuse basis functions are required.^{30,32,33,41} Even so, a strong laser field will push the electronic wave packet into regions of space where support from the atom-centered basis functions is waning, and this will manifest as spurious reflection of that wave packet by the artificial potential wall created by the lack of basis function support. To circumvent this problem, previous work on strong-field electron dynamics within an atom-centered Gaussian representation has employed a heuristic finite-lifetime model in which unbound states are given complex energies corresponding to finite lifetimes.^{31,32,41,47} As an alternative, in the present work we replace the heuristic lifetime model with the machinery of a complex absorbing potential (CAP). Such potentials are often used for the description of metastable electronic states,⁴⁸ whose wave functions are not square-integrable,^{49,50} and also as absorbing boundary conditions in wave packet quantum dynamics calculations.⁵¹ The CAP absorbs the wave packet as it reaches the edge of a finite grid or a finite basis set, thus preventing artificial interference between the outgoing and a reflected wave, the latter of which is an artifact of the finite-basis representation. The connection between CAPs and the heuristic lifetime model have been discussed elsewhere.⁴⁷ We will see that the use of a CAP is crucial to obtaining reasonable HHG spectra, as only the very lowest harmonics are well-resolved in its absence. As demonstrated herein, Gaussian-orbital-based TDKS simulations with an appropriate CAP afford high-quality HHG spectra.

II. THEORY

A. High harmonic generation

Theoretical description of HHG, including the semiclassical three-step model (Fig. 1), is discussed in detail by Ishikawa.² That material is briefly summarized here, in order to place the TDKS simulations in context. Consider a monochromatic laser pulse whose electric field is

$$E(t) = E_0 \cos(\omega_0 t) \quad (1)$$

and which is linearly polarized in the \mathbf{z} direction. For an electron that is ejected at time $t = t_{\text{ini}}$ with no initial

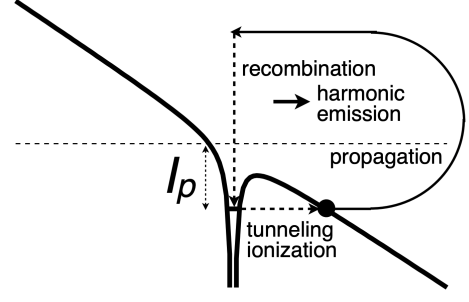


FIG. 1: Illustration of the semiclassical three-step model (ionization, propagation, and recombination) leading to HHG. Reproduced from Ref. 2 under CC BY 3.0.

velocity, setting $z(t_{\text{ini}}) = 0 = \dot{z}(t_{\text{ini}})$, one obtains²

$$z(t) = \frac{E_0}{\omega_0^2} \left[\cos(\omega_0 t) - \cos(\omega_0 t_{\text{ini}}) + (\omega_0 t_0 - \omega_0 t_{\text{ini}}) \sin(\omega_0 t_{\text{ini}}) \right]. \quad (2)$$

The kinetic energy of this electron is

$$E_{\text{KE}} = 2U_p [\sin(\omega_0 t) - \sin(\omega_0 t_{\text{ini}})]^2 \quad (3)$$

where $U_p = E_0^2/4\omega_0^2$ is the ponderomotive energy, defined as the time-averaged kinetic energy for the electron in the oscillatory laser field. A convenient formula for U_p is²

$$U_p/\text{eV} = 9.337 \times 10^{-14} \left(\frac{I}{\text{W cm}^2} \right) \left(\frac{\lambda}{\mu\text{m}} \right)^2 \quad (4)$$

where λ and I are the wavelength and the intensity of the driving field, respectively. The electron recombines with its source (see Fig. 1) at a time t_{rec} , when $z(t_{\text{rec}}) = 0$. The energy of the emitted photon created by the recombination event is

$$h\nu = E_{\text{KE}}(t_{\text{rec}}) + \text{IE} \quad (5)$$

where “IE” is the molecule’s ionization energy. The maximum photon energy (or cutoff energy, E_{cutoff}) is determined by the maximum kinetic energy in Eq. (3) under the constraint that $z(t_{\text{rec}}) = 0$ in Eq. (2). The result is a cutoff law^{2,46,52,53}

$$E_{\text{cutoff}} = c_1 U_p + c_2 \text{IE} \quad (6)$$

where c_1 and c_2 are constants. The values $c_1 = 3$ and $c_1 = 1$ are widely quoted,⁵² but more sophisticated models of the HHG process afford $c_1 = 3.17$ and $c_2 = 1.32$,⁴⁶ or else $c_1 = 3.34$ and $c_2 = 1.83$.⁵³ Defining a phase $\theta = \omega_0 t$, with an initial ($t = t_{\text{ini}}$) value θ_{ini} and a recombination ($t = t_{\text{rec}}$) value θ_{rec} , then the pair of values $\theta_{\text{ini}} + n\pi$ and $\theta_{\text{rec}} + n\pi$ also satisfy $z(\theta) = 0$, for integer values of n . The displacement z and velocity \dot{z} both

change sign every half cycle, $z(\theta) = -z(\theta - \pi)$. As a result, the harmonic field $E_{\text{HHG}}(t)$ can be expressed as²

$$E_{\text{HHG}}(t) = \cdots + f(t + 2\pi/\omega_0) - f(t + \pi/\omega_0) \\ + f(t) - f(t - \pi/\omega_0) \\ + f(t - 2\pi/\omega_0) - \cdots \quad (7)$$

for some function $f(t)$. Following a Fourier transformation, Eq. (7) has nonzero values only at odd harmonic numbers. The HHG spectrum of a molecule in a strong laser field thus consists of odd multiples of ω_0 , up to the cutoff frequency E_{cutoff}/\hbar .

B. TDKS simulations

A rigorous description of TDKS theory from first principles can be found in the work of Gross *et al.*^{19,54} and a simplified tutorial, with a discussion of contemporary problems, can be found in Ref. 23. The adiabatic approximation¹⁹ (*i.e.*, locality in time) is assumed throughout this work, so that the time dependence of the exchange-correlation functional is carried strictly by the time-evolving density, $\rho(\mathbf{r}, t)$; ground-state functionals are therefore used without alteration. The time-dependent electron density is expressed in terms of time-dependent Kohn-Sham molecular orbitals (MOs),

$$\rho(\mathbf{r}, t) = \sum_k^{\text{occ}} |\psi_k(\mathbf{r}, t)|^2. \quad (8)$$

Following a perturbation to the ground-state density, these MOs propagate in time according to the TDKS equation:

$$i\hbar \frac{d\psi_k}{dt} = \hat{F} \psi_k(\mathbf{r}, t). \quad (9)$$

This is the one-electron analogue of the time-dependent Schrödinger equation and the Fock operator \hat{F} functions as the effective Hamiltonian. The equation of motion for each ψ_k is numerically integrated to obtain time-evolving MOs $\psi_k(\mathbf{r}, t)$, starting from ground-state MOs at $t = 0$. The functions $\psi_k(\mathbf{r}, 0)$ are eigenfunctions of \hat{F} .

Equation (9) is equivalent to the Liouville-von Neumann equation

$$i\hbar \frac{d\mathbf{P}}{dt} = \mathbf{F}\mathbf{P} - \mathbf{P}\mathbf{F}, \quad (10)$$

where \mathbf{P} is the matrix representation of ρ , expressed here in an orthonormal basis that might simply be the Kohn-Sham MOs themselves. Integration of Eq. (10) affords the time-dependent density matrix, $\mathbf{P}(t)$. We express the time propagation of the latter as

$$\mathbf{P}(t + \Delta t) = \mathbf{U}(t + \Delta t, t) \mathbf{P}(t) \mathbf{U}^\dagger(t + \Delta t, t) \quad (11)$$

where $\mathbf{U}(t + \Delta t, t)$ is a unitary time-propagation operator for the time step $t \rightarrow t + \Delta t$. Because both \mathbf{P} and \mathbf{F} in

Eq. (10) are time-dependent quantities, the definition of $\mathbf{U}(t + \Delta t, t)$ involves time-ordering of the matrices $\mathbf{F}(t')$ at points t' along the integration ($t \leq t' \leq t + \Delta t$),⁵⁵ or else a Magnus expansion of nested commutators.²⁴ Various forms for $\mathbf{U}(t + \Delta t, t)$ have been discussed in previous work,²⁴ including schemes that iterate the time propagation to self-consistency over the course of a single time step from t to $t + \Delta t$. In the present work, we focus on the modified-midpoint algorithm.⁵⁶ This approach corresponds to a propagator

$$\mathbf{U}_N = \exp[-i(\Delta t) \mathbf{F}_{N+1/2}] \quad (12)$$

that updates the density matrix from t_N to $t_{N+1} = t_N + \Delta t$. The quantity $\mathbf{F}_{N+1/2}$ is the Fock matrix at $t = t_N + \Delta t/2$.

For a molecule in a laser field, the Fock operator \hat{F} consists of a field-free molecular part (\hat{F}_0) augmented with an additional term $\mathbf{E} \cdot \mathbf{r}$ involving the electric field $\mathbf{E}(t)$. In addition, we add a CAP of the form $-iW_{\text{CAP}}(\mathbf{r})$, which is discussed in detail below. These additional terms added to \hat{F}_0 both take the form of real-space potentials and the total Fock operator including these additions is

$$\hat{F} = \hat{F}_0 + \mathbf{E}(t) \cdot \mathbf{r} - iW^{\text{CAP}}(\mathbf{r}) \\ = \hat{F}' - iW^{\text{CAP}}(\mathbf{r}) \quad (13)$$

where $\hat{F}' = \hat{F}_0 + \mathbf{E}(t) \cdot \mathbf{r}$. Our implementation of the CAP is similar to that used by Schlegel and coworkers to study strong-field ionization dynamics,^{57–61} and which we have previously used to compute broadband x-ray absorption spectra.²⁵ The real-space CAP function $W^{\text{CAP}}(\mathbf{r})$ is constructed from a set of overlapping, atom-centered spherical potentials, each of which is zero within a cutoff radius r_0 then rises quadratically with curvature η . Explicitly, these functions are

$$f_k^{\text{CAP}}(\mathbf{r}) = \begin{cases} 0, & \|\mathbf{r} - \mathbf{R}_k\| < r_0 \\ \eta \|\mathbf{r} - \mathbf{R}_k\|^2, & \|\mathbf{r} - \mathbf{R}_k\| \geq r_0 \end{cases} \quad (14)$$

for $k = 1, 2, \dots, N_A$, where \mathbf{R}_k indicates the location of the k th nucleus and N_A is the number of atoms. The numerical value of $W^{\text{CAP}}(\mathbf{r})$ is taken to be the minimum value of all of the functions $f_k^{\text{CAP}}(\mathbf{r})$, except that we impose a maximum value ($E_{\text{max}} = 10$ Ha) in order to avoid numerical problems. The overall CAP function that appears in Eq. (13) is given by

$$W^{\text{CAP}}(\mathbf{r}) = \min \left\{ E_{\text{max}}, f_1^{\text{CAP}}(\mathbf{r}), \dots, f_{N_A}^{\text{CAP}}(\mathbf{r}) \right\}. \quad (15)$$

The matrix representation of W^{CAP} is required in order to propagate the Liouville-von Neumann equation. Introducing atom-centered Gaussian functions $\{g_\mu(\mathbf{r})\}$ for the atomic orbitals (AOs), this representation is

$$W_{\mu\nu}^{\text{CAP}} = \int g_\mu(\mathbf{r}) W^{\text{CAP}}(\mathbf{r}) g_\nu(\mathbf{r}) d\mathbf{r}. \quad (16)$$

The integral is evaluated by numerical quadrature, using the DFT quadrature grid.⁶² The matrix \mathbf{W}^{CAP} does not

depend on time and can be constructed once, at the beginning of a TDKS simulation, and is then added to the Fock matrix $\mathbf{F}(t)$ at each time step. Note that \mathbf{W}^{CAP} is a symmetric matrix and therefore $-\mathbf{iW}^{\text{CAP}}$ in Eq. (13) is skew-Hermitian, meaning that \mathbf{F} is not Hermitian despite the fact that \mathbf{F}_0 is real and symmetric at $t = 0$. This requires modification to the usual propagator, which is accomplished by approximate factorization of the relevant exponential, *i.e.*, the split-operator technique:⁵⁵

$$\begin{aligned} e^{-\mathbf{i}(\Delta t)\mathbf{F}} &= \exp \left[-\mathbf{i}(\Delta t)(\mathbf{F}' - \mathbf{iW}^{\text{CAP}}) \right] \\ &\approx \exp \left[-(\Delta t/2)\mathbf{W}^{\text{CAP}} \right] \exp \left[-\mathbf{i}(\Delta t)\mathbf{F}' \right] \\ &\quad \times \exp \left[-(\Delta t/2)\mathbf{W}^{\text{CAP}} \right]. \end{aligned} \quad (17)$$

In this factorization, the leading and trailing exponentials involve symmetric matrices and the middle exponential involves a skew-Hermitian matrix. Each of these can be readily diagonalized to evaluate the necessary propagator, $\exp[-\mathbf{i}(\Delta t)\mathbf{F}]$.

It is worth noting the connection between the CAP and the heuristic lifetime model introduced by Klinkusch *et al.*³¹ As noted by Coccia *et al.*,⁴⁷ adding an imaginary part to the self-consistent field (SCF) eigenvalues, $\varepsilon_p \rightarrow \varepsilon_p - \mathbf{i}\gamma_p$, formally corresponds to the use of the following CAP:

$$\mathbf{W}^{\text{CAP}}(\mathbf{r}) = \sum_p \gamma_p \psi_p^*(\mathbf{r}) \psi_p(\mathbf{r}). \quad (18)$$

(The modification is made only to the unbound states, so $\gamma_p = 0$ unless $\varepsilon_p \geq 0$.) In practice, the use of the CAP defined by Eq. (18) is more complicated as compared to that in Eq. (16) because the former depends explicitly on the MOs. We will use Eq. (16) exclusively.

In our simulations, the external field $\mathbf{E}(t) = E(t)\mathbf{n}_F$ is assumed to be linearly polarized in the direction of a unit vector \mathbf{n}_F , with

$$E(t) = G(t)A \sin(\omega_0 t) \quad (19)$$

where A and ω_0 are fixed parameters. We will explore both impulsive fields and continuous-wave fields. For the latter, the function $G(t) \equiv 1$ so that the field oscillates sinusoidally but does not decay. For the impulsive field we use a Gaussian envelope function,

$$G(t) = \exp \left(-\frac{(t - t_c)^2}{2\sigma^2} \right). \quad (20)$$

These two fields are plotted in Fig. 2 for the same parameters A and ω_0 .

The field is turned on at $t = 0$ where the MOs $\{\psi_k(\mathbf{r}, 0)\}$ represent the ground-state Kohn-Sham solution. Following sufficient time propagation, the HHG spectrum is computed from the Fourier transform ($\hat{\mathcal{F}}$) of the time-dependent dipole acceleration, $d_A(t)$.^{27,28} The dipole acceleration is the second derivative of the dipole moment, $\mu(t)$:

$$d_A(t) = \frac{d^2 \mu}{dt^2}. \quad (21)$$

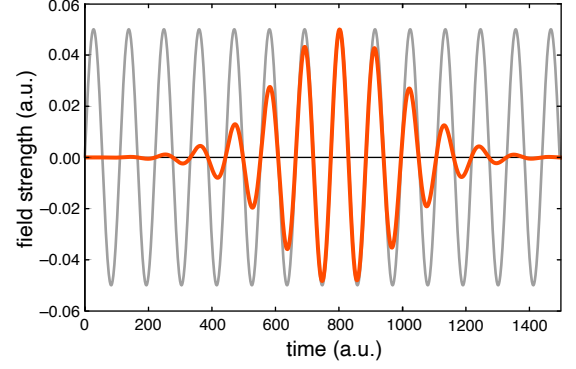


FIG. 2: An impulse field (in orange) and a continuous-wave field (in gray), as defined by $E(t)$ in Eq. (19) with different functions $G(t)$. Parameters $A = 0.05$ a.u. and $\omega_0 = 0.057$ a.u. are used in both cases and are chosen to simulate a field intensity $I = 10^{14}$ W/cm² at 800 nm. The continuous-wave field persists for the duration of the simulation while the impulse field is attenuated as shown, with parameters $t_c = 800$ a.u. and $\sigma = 200$ a.u. characterizing the Gaussian envelope in Eq. (20).

The Fourier transform of this quantity is

$$d_A(\omega) = \frac{1}{t_{\text{fin}} - t_{\text{ini}}} \int_{t_{\text{ini}}}^{t_{\text{fin}}} d_A(t) e^{-\mathbf{i}\omega t} dt. \quad (22)$$

Since the Fourier transform $[\hat{\mathcal{F}} : x(t) \mapsto X(\omega)]$ has the property

$$\hat{\mathcal{F}} \left[\frac{d^n}{dt^n} x(t) \right] = (\mathbf{i}\omega)^n X(\mathbf{i}\omega), \quad (23)$$

one may rewrite Eq. (22) as²⁸

$$d_A(\omega) = \frac{-\omega^2}{t_{\text{fin}} - t_{\text{ini}}} \int_{t_{\text{ini}}}^{t_{\text{fin}}} \mu(t) e^{-\mathbf{i}\omega t} dt, \quad (24)$$

and this is the form of $d_A(\omega)$ that is used in practice. Finally, the spectrum (or dipole oscillator strength, S) is given by^{27,28}

$$S(\omega) = \frac{3}{2\pi c^3} |d_A(\omega)|^2. \quad (25)$$

C. Computational details

Results presented here are based on a completely new implementation²⁵ of the TDKS module in Q-Chem v. 5.4,⁶³ replacing the original TDKS code written by Nguyen *et al.*^{64,65} In the new module, time propagation can be accomplished either based on the modified-midpoint algorithm,⁵⁶ which is used here, or else self-consistent predictor-corrector algorithms.²⁴

Since the HHG process involves ionization and electron recombination, the asymptotic behavior of the exchange-correlation function is crucial.²⁷⁻²⁹ We use an LRC variant of a range-separated hybrid functional,³⁹ specifically,

TABLE I: Gaussian exponents, ζ (in bohr⁻²) for hydrogen in the multiply-augmented n -aug-cc-pVTZ basis sets.

	cc-pVTZ ^a	aug-cc-pVTZ	n -aug-cc-pVTZ			
			$n = 2$	$n = 3$	$n = 4$	$n = 5$
s	1.027×10^{-1}	2.526×10^{-2}	6.210×10^{-3}	1.527×10^{-3}	3.753×10^{-4}	9.227×10^{-5}
p	3.880×10^{-1}	10.20×10^{-2}	26.80×10^{-3}	7.042×10^{-3}	18.50×10^{-4}	48.61×10^{-5}
d	10.57×10^{-1}	24.70×10^{-2}	57.70×10^{-3}	13.48×10^{-3}	31.49×10^{-4}	73.56×10^{-5}

^aSmallest exponent in the parent basis set.

the LRC- ω PBE functional with range-separation parameter $\omega = 0.3$ bohr⁻¹.³⁷ LRC functionals, as a subset of range-separated hybrid functionals,³⁹ are characterized by an asymptotic exchange functional that becomes 100% Hartree-Fock (HF) exchange for $r_{12} \gg 1/\omega$. This ensures that the asymptotic behavior of the exchange potential is $-1/r$. Not all range-separated hybrid functionals enforce the correct asymptotic behavior; see Ref. 39 for a discussion. To assess the role of electron correlation, we will also carry out some simulations at the level of TDHF theory, which is equivalent to TDKS with a functional that contains only HF exchange, with no correlation and no range separation.

Calculations are performed for H₂ at 0.75 Å separation in a spin-unrestricted formalism, with the field aligned along the internuclear axis; we take this to be polarization in the z direction, $\mathbf{n}_F = (0, 0, 1)$. The external field mimics a laser field with intensity of $I = 10^{14}$ W/cm² and carrier frequency $\omega_0 = 1.55$ eV ($= 800$ nm). In atomic units, this corresponds to $A = 0.05$ a.u. and $\omega_0 = 0.057$ a.u. in Eq. (19). For the Gaussian-impulse field [Eq. (20)], we take $t_c = 800$ a.u. and $\sigma = 200$ a.u., and use a total simulation time of 1500 a.u. (≈ 36.3 fs), extending just beyond the support of the envelope function $E(t)$ for this set of parameters. We also report simulations using a continuous-wave field where the total simulation time is 5,000 a.u. (≈ 121 fs). These simulations use the same values A and ω_0 that define the impulsive field, so that the peak value of $E(t)$ is the same in both cases. (Both fields are plotted in Fig. 2.) At low field intensities, vibrational motion may destroy coherences needed to obtain the highest harmonic orders⁶⁶ but is not considered here, where we use an ionizing field intensity.

The shape of the CAP is described by Eq. (14) with various values of the turn-on radius r_0 , in a range from 4.0–18.5 bohr. The curvature parameter η is tested within a range 0.4–4.0 Ha/bohr². The time propagation algorithm is described in Section II B and the time step is $\Delta t = 0.1$ a.u.. In performing the Fourier transform that is indicated in Eq. (24), a Hann window function, $w(t) = \sin^2[\pi t/(t_{\text{fin}} - t_{\text{ini}})]$, is applied to the time series of $\mu(t)$ data.

The basis set for all calculations is 5-aug-cc-pVTZ, which has been shown to afford a good balance of convergence versus cost in TD-CIS simulations of HHG spectra in H₂.³² This basis set is constructed by adding four additional sets of s , p , and d diffuse functions to the

TABLE II: Gaussian half-widths at half-maximum (HWHM, in bohr) for the most diffuse basis function on hydrogen.

	cc-pVTZ	n -aug-cc-pVTZ				
		$n = 1^a$	$n = 2$	$n = 3$	$n = 4$	$n = 5$
s	2.60	5.24	10.57	21.31	42.98	86.68
p	1.34	2.61	5.09	9.92	19.36	37.76
d	0.81	1.68	3.47	7.17	14.84	30.70

^aConventional aug-cc-pVTZ basis set.

conventional aug-cc-pVTZ basis set.⁶⁷ Exponents ζ for these additional functions are provided in Table I. Those exponents are converted into radial half-widths at half-maximum (HWHM) in Table II, where⁵⁰

$$\text{HWHM}(\zeta) = \frac{\sqrt{\ln 2}}{\zeta^{1/2}} \approx 0.8326 \zeta^{-1/2}. \quad (26)$$

Values of $\text{HWHM}(\zeta)$ make it easy to understand the radial extent of each n -aug-cc-pVTZ basis set. The one that we use ($n = 5$) includes s functions extending out to $\text{HWHM} \approx 87$ bohr or 46 Å. The use of functions this diffuse can lead to numerical linear dependency problems if thresholds are set too loose. We convergence the initial ground-state SCF calculation using an energy threshold of 10^{-9} Ha and integral thresholds are set to 10^{-12} a.u. for all Fock builds.

III. RESULTS AND DISCUSSION

We first verify that the value $\Delta t = 0.1$ a.u. is suitable to obtain a stable simulation. Using the impulse field that is plotted in Fig. 2, we performed a TDKS simulation using values of Δt ranging from $\Delta t = 0.01$ a.u. ($= 0.242$ as), corresponding to a Nyquist frequency of 8.5 keV,^{24,25} up to as large as $\Delta t = 0.2$ a.u. ($= 4.84$ as), corresponding to a Nyquist frequency of 427 eV. Since the external field is applied in the z direction, corresponding to the internuclear axis of H₂, we can use $\mu_z(t)$ to assess the impact of Δt . This quantity is plotted in Fig. 3 for simulations using three different time steps and the results track one another quite well. Taking the smallest time step ($\Delta t = 0.01$ a.u.) as the benchmark, differences in μ_z for the larger time-step simulations are on the order of 10^{-4} a.u., in a total dipole moment whose magnitude ranges almost to 0.4 a.u.. If the time step is increased to $\Delta t = 0.2$ a.u. then the deviations in μ_z increase in mag-

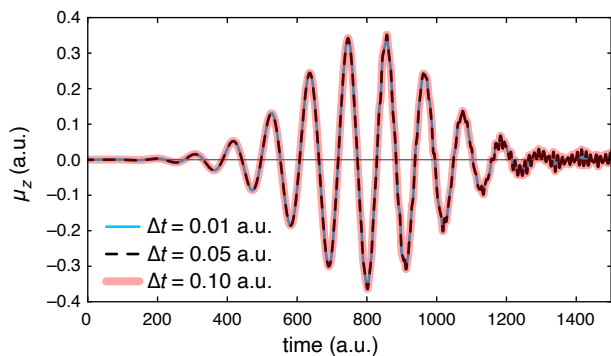


FIG. 3: Time-dependent dipole moment $\mu_z(t)$ for the H_2 molecule, obtained from TDKS simulations at the LRC- ω PBE/5-aug-cc-pVTZ level using various time steps, Δt . The simulations use the impulse field shown in Fig. 2.

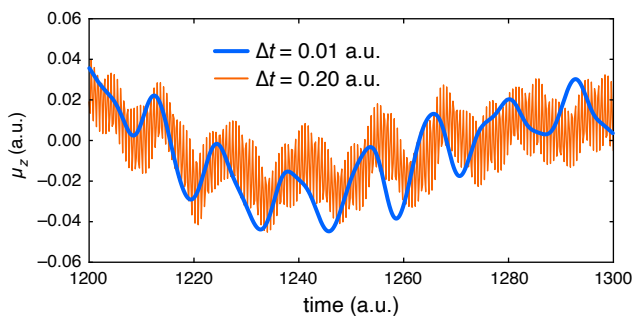


FIG. 4: Time-dependent dipole moment $\mu_z(t)$ for the H_2 molecule, obtained from TDKS simulations at the LRC- ω PBE/5-aug-cc-pVTZ level with two different time steps. The simulations use the impulse field shown in Fig. 2 and the $\Delta t = 0.01$ a.u. data are the same as those plotted in Fig. 3. For clarity, only a portion of the simulation is shown but these simulations have the same $t = 0$ starting point as those in Fig. 3.

nitude to $\sim 10^{-2}$ a.u. and some spurious high-frequency oscillations appear (Fig. 4). As such, $\Delta t = 0.1$ a.u. is the best choice for accuracy and efficiency.

Figure 5 presents HHG spectra for H_2 computed using TDKS simulations with both the LRC- ω PBE functional as well as TDHF theory. In this first set of numerical control experiments, no CAP is applied and the laser field is the same impulse field that was used for the stability tests, with a total time propagation of 1,500 a.u.. Neither spectrum in Fig. 5 conveys much of the known characteristics of a high-harmonic spectrum, in concurrence with previous TD-CIS simulations when no correction for the unbound states is applied.³² Only the first three harmonics are well resolved in the DFT spectrum and only the first two harmonics in the HF spectrum.

The high-harmonic cutoff energy can be calculated using $U_p = 5.98$ eV, which comes from Eq. (4) with the field parameters $I = 10^{14}$ W/cm² and $\lambda = 800$ nm. The IE ranges from 14.3–16.3 eV, depending on whether the Δ SCF value is used or the Koopmans' value (IE =

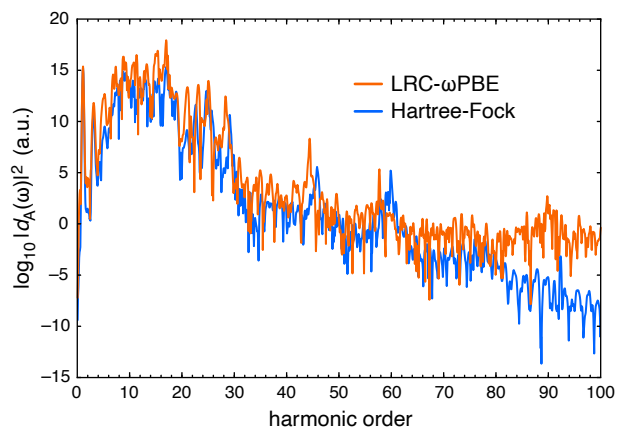


FIG. 5: HHG spectra for H_2 computed using the TDKS approach with two different functionals and no CAP, using the 5-aug-cc-pVTZ basis set in both cases. An impulsive field is applied, with parameters as in Fig. 2, and the simulations are propagated for 1,500 a.u. in time. The vertical axis shows the signal $|d_A(\omega)|^2$ on a logarithmic scale. The horizontal axis is the harmonic order, in multiples of the fundamental frequency $\omega_0 = 1.55$ eV = 800 nm.

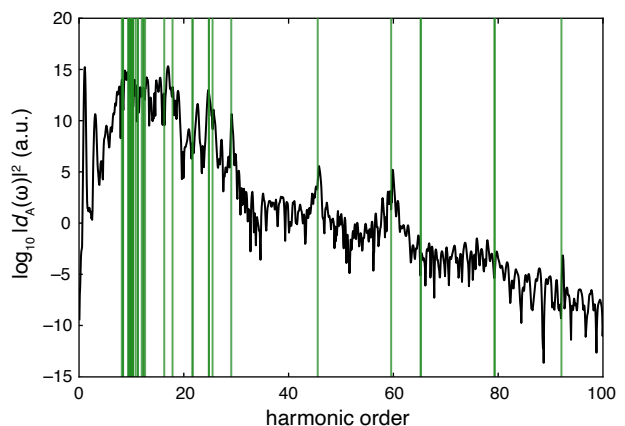


FIG. 6: HHG spectrum of H_2 computed at the HF/5-aug-cc-pVTZ level from an impulsive simulation (in black, corresponding to the TDHF data from Fig. 5), overlaid with vertical excitation energies (in green) computed from a LR-TDHF calculation. Only LR-TDHF transitions with nonzero oscillator strength are shown. Vertical sticks in darker green correspond to overlapping transitions. The vertical axis shows the HHG signal $|d_A(\omega)|^2$ on a logarithmic scale and the horizontal scale is in multiples of the fundamental frequency, $\omega_0 = 1.55$ eV.

$-\epsilon_{\text{HOMO}}$), and depending on whether the level of theory is HF or LRC- ω PBE. (The 5-aug-cc-pVTZ basis set is used in each case.) Using the most recent estimate of the cutoff energy,⁵³ namely, Eq. (6) with $c_1 = 3.34$ and $c_2 = 1.83$, one obtains values of E_{cutoff} ranging from 46.1–49.8 eV, corresponding to 30–32 harmonics. In the context of TDKS calculations it is probably more appropriate to use the Koopmans' value of the IE because

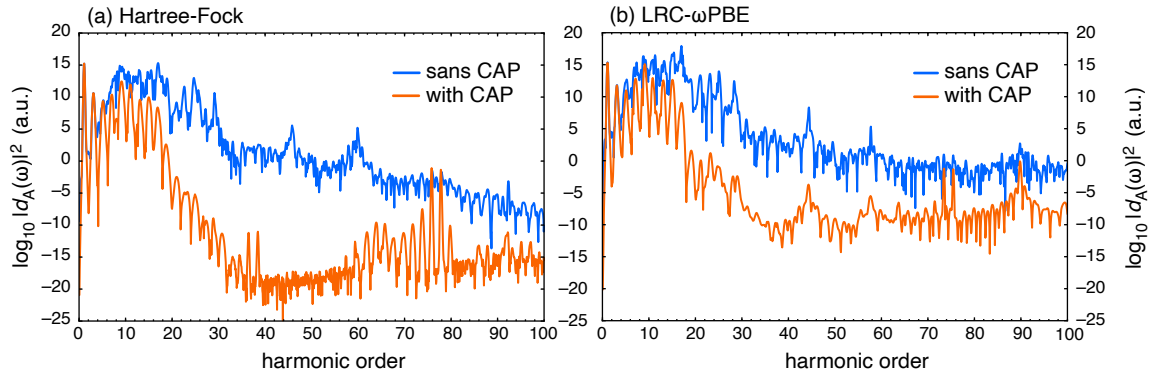


FIG. 7: Comparison of HHG spectra for H_2 computed from simulations with and without a CAP, using (a) TDHF theory and (b) TDKS with the LRC- ω PBE functional. The field is an impulse (Fig. 2) and all simulations are propagated for 1,500 a.u. in time. CAP parameters are set to $r_0 = 9.524$ bohr ($= 18.00$ Å) and $\eta = 4.0$ Ha/bohr². The vertical scale is logarithmic and the horizontal axis is in units of the fundamental frequency, $\omega_0 = 1.55$ eV.

excitations into unbound MOs afford ionization channels. Taking $IE = -\epsilon_{HOMO}$, the cutoff is estimated around the 30th harmonic for LRC- ω PBE or the 32nd harmonic for HF.

The sharp drop in intensity that is observed in the HHG spectra of Fig. 5 is thus in good agreement with the cutoff estimate in Eq. (6). However, in the TDKS simulations the intensity does persist to higher harmonic orders, albeit much attenuated, and there are spikes in intensity (corresponding to fictitious harmonics) around the 45th and 60th harmonic orders. We hypothesize that this behavior results from artificial confinement of the electron due to the finite extent of the Gaussian basis set. Higher-energy parts of the outgoing wave that should be ionized are instead confined and reflected, generating spurious interference features and generally contributing to a noisy spectrum.

To confirm this hypothesis, Fig. 6 overlaps the HHG spectrum computed at the TDHF level with an excitation spectrum computed using linear response (LR) TDDFT. (We use LR-TDHF and thus compare to the TDHF data from Fig. 5. For clarity, only the LR-TDHF states with oscillator strengths greater than 1×10^{-10} are shown.) It is apparent that the enhanced high-harmonic intensity around the 45th and 60th harmonic orders coincides with LR-TDDFT excitation energies having nonzero oscillator strengths. Thus, we conclude that these are enhancements in the high-harmonic spectrum driven by resonances with excited states of the system, but are not physically reasonable because the excited states in question lie well above the ionization threshold and are thus bound only by the finite support of the Gaussian basis set that prevents the molecule from ionizing. Note that the LR-TDDFT calculation exhibits resonances coinciding already with the 4th harmonic in the HHG spectrum and these may also be responsible for the lack of resolution that is observed in the TDKS simulations in Fig 5, even at lower harmonic orders.

We thus turn to TDKS simulations using a CAP. Fig-

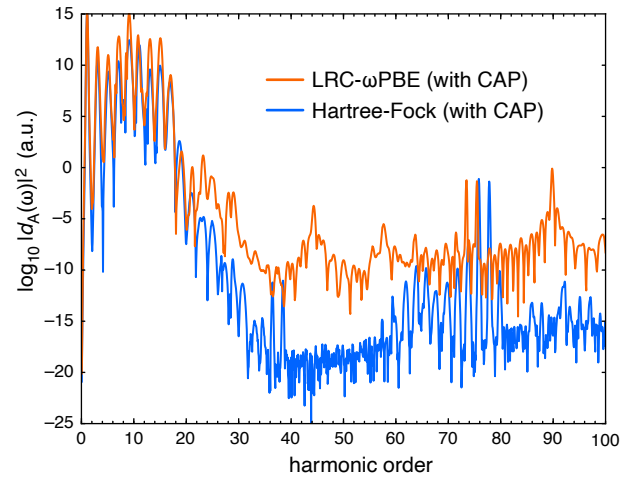


FIG. 8: Comparison of HHG spectra for H_2 computed from TDKS versus TDHF simulations, both of which use a CAP. The field is impulsive impulse (see Fig. 2) and all simulations are propagated for 1,500 a.u. in time. These are the same spectra that were plotted in Fig. 7 but placed side-by-side here, omitting the results obtained sans CAP. The CAP parameters are set to $r_0 = 9.524$ bohr ($= 18.00$ Å) and $\eta = 4.0$ Ha/bohr².

ure 7 presents a side-by-side comparison of the HHG spectra computed with and without a cap. At both the HF and LRC- ω PBE levels of theory, the noise in the original spectrum (sans CAP) is greatly reduced and consequently distinct peaks emerge at odd harmonic orders, as anticipated. The two spectra (HF and LRC- ω PBE) computed with a CAP are compared side-by-side in Fig. 8. Up to the 20th harmonic, the TDHF and TDKS results match relatively well but the TDHF spectrum subsequently falls off much more rapidly between the 20th and 30th harmonics. Above the 30th harmonic, the LRC- ω PBE spectrum continues to exhibit markedly larger intensity. There are also some resurgent peaks

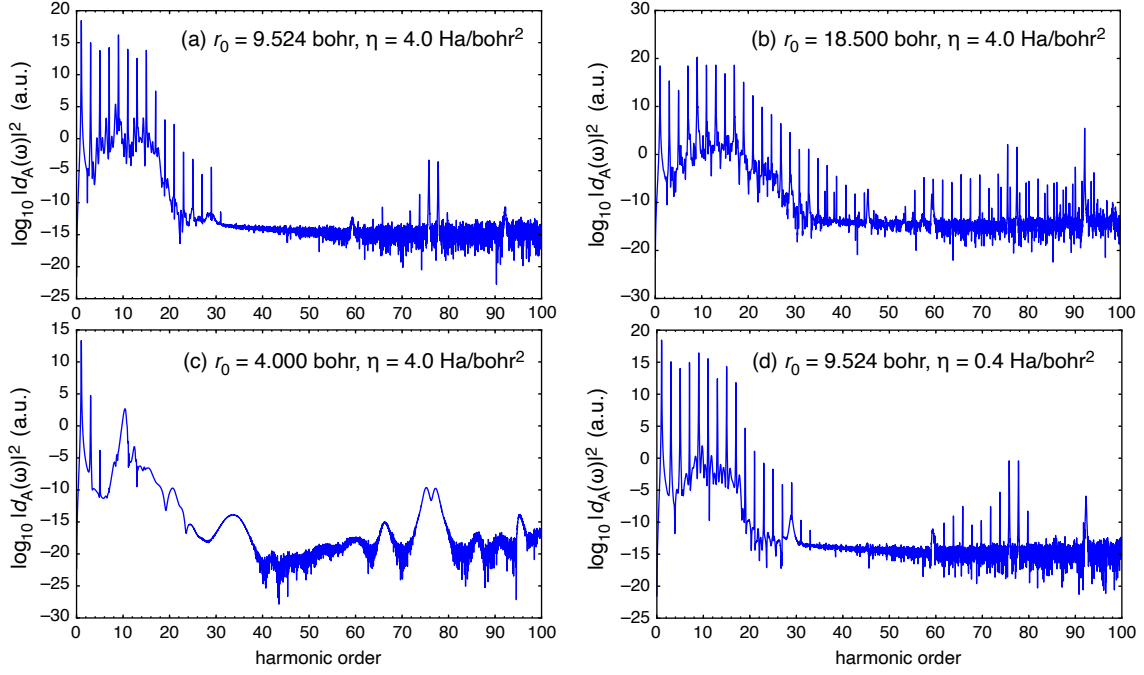


FIG. 9: Comparison of HHG spectra for H_2 computed at the TDHF/5-aug-cc-pVTZ level using various values of the parameters r_0 and η that define the CAP, as indicated. All four simulations were performed using a continuous wave field (see Fig. 2) and 5,000 a.u. of time propagation. The vertical scale (which is logarithmic) is different in each panel.

in both spectra, between the 70th and 80th harmonics, which are discussed below. Due to the logarithmic scale on which all of these HHG spectra are plotted, differences between the TDHF and TDKS results above the 30 harmonic order are generally $< 10^{-6}$ on an absolute intensity scale, which is small considering that the major peaks at low harmonic orders are $\sim 10^{+10}$ – 10^{+15} on the same scale.

Figure 9 shows HHG spectra computed at the HF/5-aug-cc-pVTZ level using four different CAPs, defined by different choices of the parameters r_0 and η in Eq. (14). Unlike the previous simulations, each of which used an impulsive field and were propagated for 1,500 a.u., these simulations used a continuous-wave field and were propagated for 5,000 a.u. Figure 9a uses the same set of CAP parameters as in Fig. 8 and we will use this spectrum as a reference in examining the effects of the CAP parameters. As compared to the simulation using an impulsive field (Fig. 8), the corresponding simulation with a continuous wave (Fig. 9a) provides a much better resolved set of peaks all the way up to the anticipated harmonic cutoff, because the system experience more cycles of the laser field. Beyond the 30th harmonic the intensity drops dramatically and the baseline is reduced by several orders of magnitude as compared to the corresponding simulation using an impulsive field. Fictitious peaks around the 60th, 75th, and 93rd harmonic orders can be observed in both simulations, but their intensity is reduced in the continuous-wave calculation.

As compared to that in Fig. 9a, the spectrum reported

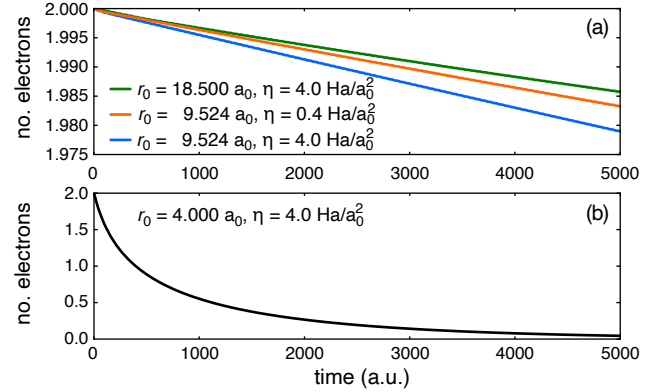


FIG. 10: Ionization rates for the simulations in Fig. 9, computed at the TDHF/5-aug-cc-pVTZ level with a continuous-wave field: (a) CAP parameter sets (r_0, η) leading to slow ionization, versus (b) a much smaller value of r_0 that affords a much larger ionization rate and annihilates the entire electron density over the course of 5,000 a.u. of time propagation.

in Fig. 9b is computed using the same value of η but a much larger value of r_0 . The result is that the harmonic progression no longer drops nearly as precipitously at the 30th harmonic, as it does for the smaller turn-on radius, but persists all the way to the 100th harmonic. Alongside the anticipated odd harmonics are a set of spurious, parallel features. Conversely, when r_0 is reduced to 4.0 bohr (Fig. 9c), keeping η the same, the result is that

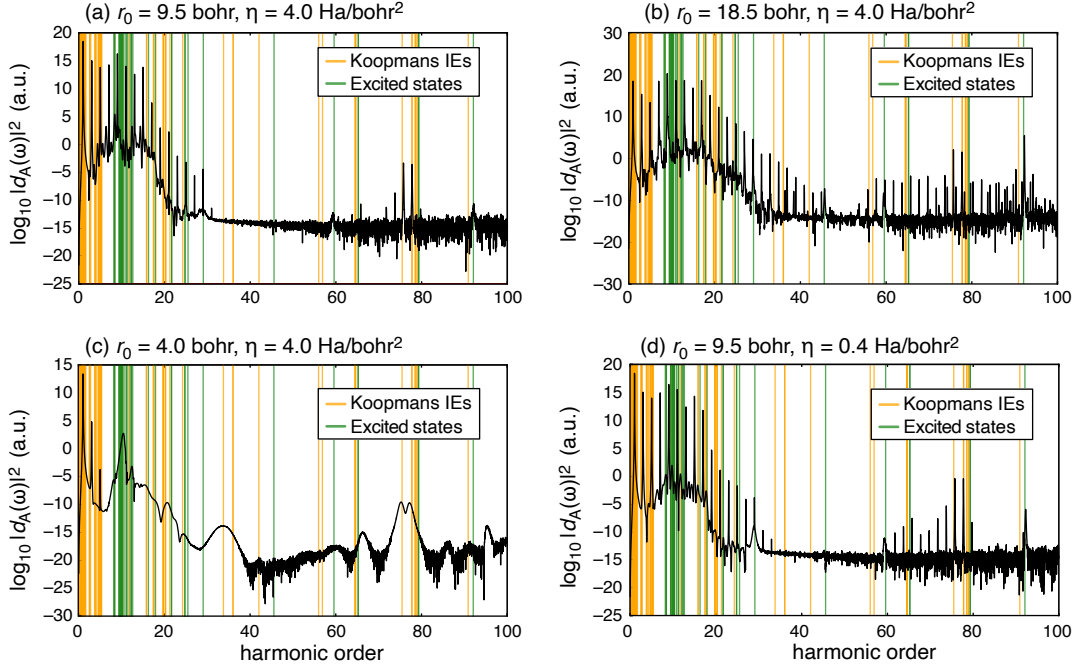


FIG. 11: HHG spectra for H_2 , computed at the TDHF level using various values of the CAP parameters r_0 and η . Simulations were performed for 5,000 a.u. of time propagation under a continuous wave and the HHG spectra are the same ones that are reported in Fig. 9, but are overlaid here with vertical lines representing the Koopmans' theorem IEs ($-\varepsilon_k$ where ε_k is an occupied energy level, in translucent orange) and LR-TDHF excited states (in translucent green). Darker colored vertical lines indicate overlapping transitions in the stick spectra.

the low-order harmonics disappear beyond the third one. Together, these simulations set boundaries on acceptable values of r_0 : the largest value ($r_0 = 18.500$ bohr) fails to attenuate the harmonics at the expected cutoff while the smallest value ($r_0 = 4.000$ bohr) attenuates the signal so much that nearly all of the harmonics are swallowed by the absorbing potential. Finally, Fig. 9d uses $r_0 = 9.524$ bohr (as in Fig. 9a) but reduces the curvature η by a factor of 10. This choice restores the harmonic cutoff around 30th order but the spectrum exhibits spurious peaks above the 60th harmonic order, and these are somewhat stronger than they were for the larger value of η with the same turn-on radius.

Figure 10 plots the ionization rates for the simulations in Fig. 9. For the three sets of CAP parameters (r_0, η) leading to clear HHG peaks (Figs. 9a, b, and d), the ionization rates are plotted together in Fig. 10a and are rather slow, such that only ≈ 0.02 electrons are lost over the course of 5,000 a.u. of time propagation. The ionization rate is much larger when $r_0 = 4.0$ bohr (Fig. 10b), such that the entire electron density is annihilated by the CAP over the course of 5,000 a.u. of time propagation. The corresponding HHG spectrum is shown in Fig. 9c and fails to evince any clear harmonics beyond the first three, and two of those are severely attenuated. The conclusion is that the CAP plays a critical role in obtaining characteristic HHG spectra, as without it the spectra are overwhelmed by noise and higher harmonics are miss-

ing. The 1% of the electron density that is annihilated in Fig. 10a is critical to obtaining a clean HHG spectrum, for otherwise this part of the density becomes a reflected wave whose interference with the outgoing wave leads to noise in the spectrum. On the other hand, if the turn-on radius of the CAP is set too close to the nuclei (small r_0), then the electron density is absorbed too quickly and the system does not experience enough pulse cycles to generate well-resolved harmonics.

In Fig. 11, the HHG spectra from Fig. 9 are plotted again, along with Koopmans IEs and LR-TDHF excitation energies, both as stick spectra. For clarity, only excited states with nonzero oscillator strengths (greater than 1×10^{-10}) are shown, as these should dominate the transition rate and are sufficient to illustrate the fact that some spurious features in the HHG spectrum coincide with physical excitation energies. Specifically, fictitious peaks between the 60th and 80th harmonic orders are observed to coincide with Koopmans IEs, $-\varepsilon_k$ (where ε_k is an occupied energy level). Particularly revealing is the spectrum computed using $r_0 = 4.0$ bohr (Fig. 11c), where the ionization is rapid. A broad feature around the 30th harmonic order coincides with a particular Koopmans IE, as does another broad feature around the 70th harmonic. (Note that the MO energy levels are much more sparse after the 30th harmonic order, as compared to the low-energy regime.) We conclude from this that these ionizable MOs do provide ionization channels if the

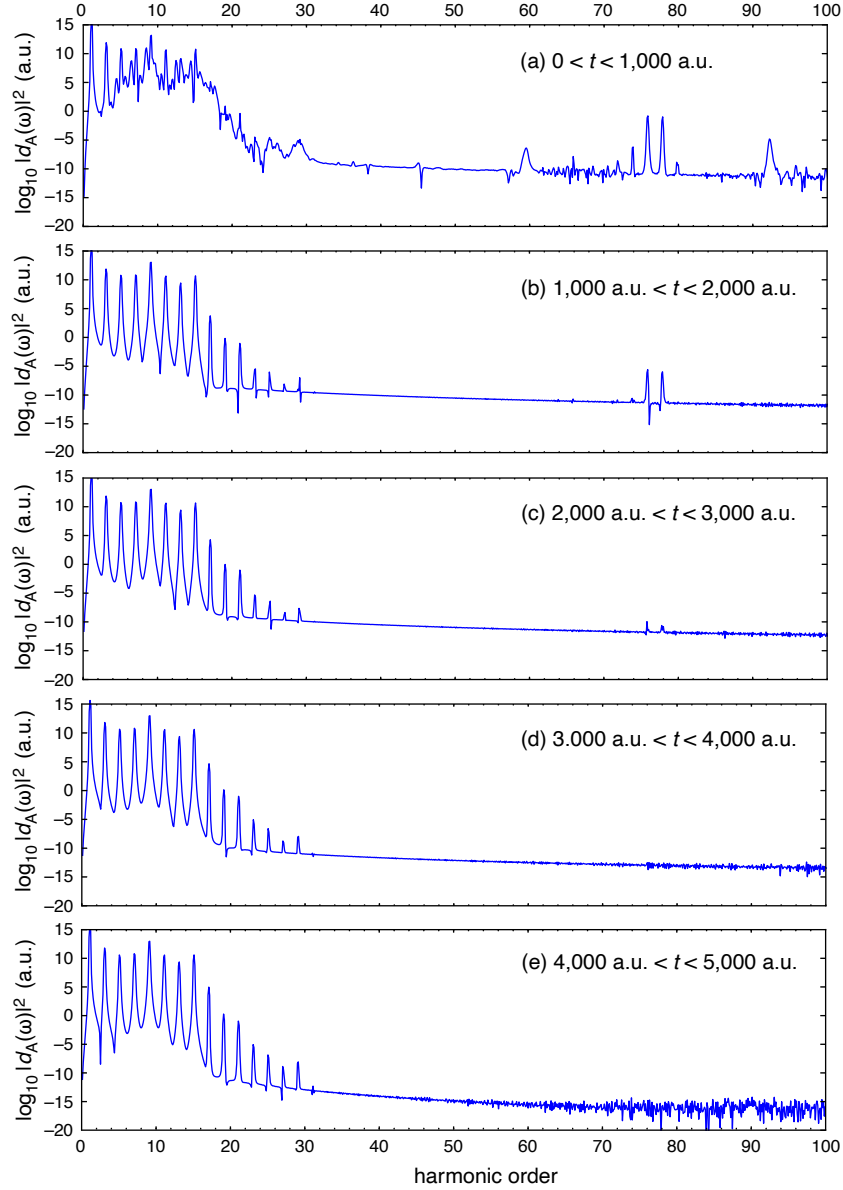


FIG. 12: HHG spectra for H_2 computed at the TDHF/5-aug-cc-pVTZ level from a continuous-wave simulation with CAP parameters $r_0 = 9.524$ bohr and $\eta = 4.0$ Ha/bohr². The total simulation time of 5,000 a.u. has been divided into five consecutive segments of 1,000 a.u. each and the spectra in panels (a)–(e) are obtained from the Fourier transform of the dipole moment data within each segment, as indicated. The intensity scale, which is logarithmic, is the same in each panel.

field-perturbed density has enough overlap with the CAP. Contrasting this behavior is the spectrum computed using $r_0 = 18.5$ bohr (Fig. 11b), which exhibits fictitious peaks at precisely the same energies, albeit very narrow ones, and well-defined features in the HHG spectrum are still obtained at energies well above these ionization channels and well above the predicted cutoff energy. According to Table II, there are a total of 23 basis functions whose HWHM exceeds 9.5 bohr, and 14 basis functions where the HWHM is greater than 18.5 bohr. We conclude that $r_0 = 18.5$ bohr does not have good overlap with the atom-centered basis functions and the nonzero

regions of the CAP reside largely outside of the region that has basis function support.

As compared to the large- r_0 spectrum in Fig. 11b, the small- η spectrum in Fig. 11d exhibits a smaller region of narrow fictitious peaks. The parameter η determines the strength of the CAP and its smaller value in Fig. 11d as compared to Fig. 11a (with $r_0 = 9.524$ bohr in both cases) leads to additional peaks above the cutoff energy when η is smaller. In the simulation with the smaller value of η , some of these above-cutoff peaks coincide with excitation energies computed using LR-TDHF theory, indicating that there are resonances that persists and con-

tribute to interference in the spectrum that is eliminated at the larger value of η .

Focusing now on the spectrum with CAP parameters $r_0 = 9.524$ bohr and $\eta = 4.0$ Ha/bohr², Fig. 12 shows several different versions of this spectrum computed from “windowed” Fourier transforms in which the total time propagation of 5,000 a.u. is divided into five sequential segments and the transform is computed using only the data from within one segment. For the segment corresponding to $0 < t < 1,000$ a.u. (Fig. 12a), peaks are obtained at the odd harmonic numbers but they are not yet very clear or sharp, and fictitious peaks are obtained starting from the 60th harmonic order and continuing through the 100th order. Significant peaks near the 60th and 93rd harmonic orders clearly correspond to LR-TDHF excited states. Unphysical peaks between the 75th and 80th harmonic orders correspond to ionization channels as inferred from the MO eigenvalues.

Within the second data segment (Fig. 12b), corresponding to the next 1,000 a.u. of time propagation, peaks become clearer and sharper at the anticipated odd harmonic orders, up to about the 30th harmonic that corresponds to the expected cutoff energy. The region of fictitious peaks shrinks dramatically, as compared to the spectrum computed within the first 1,000 a.u. of propagation time, and no fictitious peaks are observed until the 75th harmonic order. Unphysical features due to TDHF excited states that were observed in the first data segment are gone, and the remaining fictitious peaks (between the 75th and 80th harmonic orders) are smaller than what was observed from the first segment of simulation data. In the third segment (Fig. 12c), the spectrum is cleaner still and the spurious peaks between the 75th and 77th harmonic orders are quite small. These features completely disappear from spectra computed from the next data segment, corresponding to 3,000 a.u. $< t < 4,000$ a.u. (Fig. 12d). This remains true in the final data segment (4,000 a.u. $< t < 5,000$ a.u., in Fig. 12e), although the high-energy tail becomes more noisy.

The success of this windowing procedure can be interpreted as follows. In the case that the basis set was complete and covered all of space extending to infinity, then some part of the H₂ wave packet would quickly be ionized by the strong laser field, never to return. In practice, the finite extent of the basis set means that there are spurious peaks corresponding to excitations into unbound states, the rate of which is dominated by the first-order transition integrals and the most significant spurious features coincide with excited states having nonzero oscillator strength. By windowing the spectrum, we only include $\mu(t)$ data from later times in the Fourier transform, by which time some of the high-frequency, artificially-trapped electron wave has been absorbed by the CAP.

IV. SUMMARY AND CONCLUSIONS

Based on a new implementation of the TDKS or “real-time TDDFT” method in the Q-Chem code,^{25,63} we have tested the TDKS approach for simulation of high harmonic spectra using atom-centered Gaussian basis functions and an atom-centered, real-space CAP. In these strong-field simulations, the CAP serves to absorb the highest-energy part of the outgoing charge density wave, representing tunneling ionization, which would otherwise reflect off of the artificial barrier that is created by the finite extent of the basis set. Interference between the outgoing and reflected waves then leads to significant noise in the high harmonic spectrum obtained from the fluctuating dipole moment function.

In this preliminary report, we have characterized the CAP parameters that are needed to obtain a well-defined harmonic progression that terminates at the appropriate energy cutoff, without spurious peaks at high energy. Absent the CAP, only a few low-energy harmonics can be observed but even when the CAP is activated, spurious peaks may result (coinciding with certain resonances) if the CAP parameters r_0 and η are not set properly. Some of these spurious peaks coincide with excitation energies while other result from ionization channels coinciding with Koopmans ionization energies, $-\varepsilon_k$. We find that the turn-on radius for the CAP (parameter r_0) primarily affects the cutoff energy at which the harmonic sequence is attenuated, while the curvature parameter (η) controls the noise in the spectrum. Since the cutoff energy can be estimated in advance, the value of r_0 should be modified on this basis. The value of η can then be set to control the noise above the harmonic cutoff.

The use of atom-centered basis functions (as opposed to real-space grids), and a commensurate atom-centered CAP that requires only standard, atom-centered DFT quadrature grids,⁶² makes the present methodology extensible to larger molecular systems, perhaps including models of condensed-phase systems. The cost of a single TDKS time step is comparable to the cost of a ground-state SCF cycle and the memory footprint is only twice that of a ground-state DFT calculation, due to the use of complex-valued matrices. The Gaussian orbital representation is thus essential for extending strong-field calculations to polyatomic molecules, and others have already reported applications including HHG spectra of CH₂Cl₂,⁶⁸ as well as strong-field ionization rates of C₆H₈,⁵⁷ both at the TD-CIS level. The present formalism suggests an efficient means to add correlation to those calculations, as an alternative to time-dependent implementations of correlated wave function models.⁶⁹ In moving to larger systems, one may need to deal with a linear dependency problem arising when very diffuse basis sets are employed (such as 5-aug-cc-pVTZ that is used here), which we circumvent in the present work using very tight thresholds. Judicious use of floating centers (“ghost atoms”) may be an alternative means to circumvent this problem. This extensibility may open the door

to simulations of strong-field phenomena in a wide variety of complex systems.

Acknowledgements

This work was supported by the National Science Foundation under grant nos. CHE-1665322 and CHE-

1955282. Calculations were performed at the Ohio Super Computer Center under project no. PAS-0003.⁷⁰ J.M.H. serves on the board of directors of Q-Chem, Inc.

- ¹ F. Krausz and M. Ivanov, “Attosecond physics”, *Rev. Mod. Phys.*, **81**, 163–234 (2009).
- ² K. L. Ishikawa, “High-harmonic generation”, in *Advances in Solid State Lasers: Development and Applications*, M. Grishin, Ed.; IntechOpen: Croatia, 2010.
- ³ T. Popmintchev, M.-C. Chen, D. Popmintchev, P. Arpin, S. Brown, S. Ališauskas, G. Andriukaitis, T. Balčiūnas, O. D. Mücke, A. Pugzlys, A. Baltuška, B. Shim, S. E. Schrauth, A. Gaeta, C. Hernández-García, L. Plaja, A. Becker, A. Jaron-Becker, M. M. Murnane, and H. C. Kapteyn, “Bright coherent ultrahigh harmonics in the keV x-ray regime from mid-infrared femtosecond lasers”, *Science*, **336**, 1287–1291 (2012).
- ⁴ A. S. Johnson, T. Avni, E. W. Larsen, D. R. Austin, and J. P. Marangos, “Attosecond soft x-ray high harmonic generation”, *Phil. Trans. R. Soc. A*, **377**, 20170468:1–12 (2019).
- ⁵ L. Miaja-Avila, G. C. O’Neil, J. Uhlig, C. L. Cromer, M. L. Dowell, R. Jimenez, A. S. Hoover, K. L. Silverman, and J. N. Ullom, “Laser plasma x-ray source for ultrafast time-resolved x-ray absorption spectroscopy”, *Struct. Dynam.*, **2**, 024301:1–12 (2015).
- ⁶ R. Schoenlein, T. Elsaesser, K. Holidack, Z. Huang, H. Kapteyn, M. Murnane, and M. Woerner, “Recent advances in ultrafast x-ray sources”, *Phil. Trans. R. Soc. A*, **377**, 20180384:1–37 (2019).
- ⁷ R. Geneaux, H. J. B. Marroux, A. Guggenmos, D. M. Neumark, and S. R. Leone, “Transient absorption spectroscopy using high harmonic generation: A review of ultrafast x-ray dynamics in molecules and solids”, *Phil. Trans. R. Soc. A*, **377**, 20170463:1–27 (2019).
- ⁸ A. Depresseux, E. Oliva, J. Gautier, F. Tissandier, J. Nejdl, M. Kozlova, G. Maynard, J. P. Goddet, A. Tafzi, A. Lifschitz, H. T. Kim, S. Jacquemot, V. Malka, K. T. Phuoc, C. Thaur, P. Rousseau, G. Iaquaniello, T. Lefrou, A. Flacco, B. Vodungbo, G. Lambert, A. Rousse, P. Zeitoun, and S. Sebban, “Table-top femtosecond x-ray laser by collisional ionization gating”, *Nat. Photonics*, **9**, 817–822 (2015).
- ⁹ C. Kleine, M. Ekimova, G. Goldsztejn, S. Raabe, C. Strüber, J. Ludwig, S. Yarlagadda, S. Eisebitt, M. J. J. Vrakking, T. Elsaesser, E. T. J. Nibbering, and A. Rouzée, “Soft x-ray absorption spectroscopy of aqueous solutions using a table-top femtosecond soft x-ray source”, *J. Phys. Chem. Lett.*, **10**, 52–58 (2019).
- ¹⁰ A. D. Smith, T. Balčiūnas, Y.-P. Chang, C. Schmidt, K. Zinchenko, F. B. Nunes, E. Rossi, V. Svoboda, Z. Yin, J.-P. Wolf, and H. J. Wörner, “Femtosecond soft-x-ray absorption spectroscopy of liquids with a water-window high-harmonic source”, *J. Phys. Chem. Lett.*, **11**, 1981–1988 (2020).
- ¹¹ F. Lépine, “Short-pulse physics”, in *Fundamentals of Time-Dependent Density Functional Theory*, M. A. L. Marques, N. T. Maitra, F. M. S. Nogueira, E. K. U. Gross, and A. Rubio, Eds., Vol. 837 of *Lecture Notes in Physics*; Springer-Verlag: Berlin, 2012; chapter 1, pages 3–14.
- ¹² C. A. Ullrich and A. D. Bandrauk, “Atoms and molecules in strong laser fields”, in *Fundamentals of Time-Dependent Density Functional Theory*, M. A. L. Marques, N. T. Maitra, F. M. S. Nogueira, E. K. U. Gross, and A. Rubio, Eds., Vol. 837 of *Lecture Notes in Physics*; Springer-Verlag: Berlin, 2012; chapter 18, pages 351–371.
- ¹³ K. Ramasesha, S. R. Leone, and D. M. Neumark, “Real-time probing of electron dynamics using attosecond time-resolved spectroscopy”, *Annu. Rev. Phys. Chem.*, **67**, 41–63 (2016).
- ¹⁴ L. S. Cederbaum and J. Zobeley, “Ultrafast charge migration by electron correlation”, *Chem. Phys. Lett.*, **307**, 205–210 (1999).
- ¹⁵ A. I. Kuleff, N. V. Kryzhevoi, M. Pernpointner, and L. S. Cederbaum, “Core ionization initiates subfemtosecond charge migration in the valence shell of molecules”, *Phys. Rev. Lett.*, **117**, 093002:1–5 (2016).
- ¹⁶ P. N. Kraus and H. J. Wörner, “Perspectives of attosecond spectroscopy for the understanding of fundamental electron correlations”, *Angew. Chem. Int. Ed. Engl.*, **57**, 5228–5247 (2018).
- ¹⁷ A. Palacios and F. Martín, “The quantum chemistry of attosecond molecular science”, *WIREs Comput. Mol. Sci.*, **10**, e1430:1–28 (2020).
- ¹⁸ C. Ullrich, *Time-Dependent Density-Functional Theory: Concepts and Applications*, Oxford University Press: New York, 2012.
- ¹⁹ E. K. U. Gross and N. T. Maitra, “Introduction to TDDFT”, in *Fundamentals of Time-Dependent Density Functional Theory*, M. A. L. Marques, N. T. Maitra, F. M. S. Nogueira, E. K. U. Gross, and A. Rubio, Eds., Vol. 837 of *Lecture Notes in Physics*; Springer-Verlag: Heidelberg, 2012; chapter 1, pages 53–97.
- ²⁰ F. Furche, “On the density matrix based approach to time-dependent density functional response theory”, *J. Chem. Phys.*, **114**, 5982–5992 (2001).
- ²¹ A. Dreuw and M. Head-Gordon, “Single-reference ab initio methods for the calculation of excited states of large molecules”, *Chem. Rev.*, **105**, 4009–4037 (2005).
- ²² Y. Kawashita, T. Nakatsukasa, and K. Yabana, “Time-dependent density-functional theory simulation for electron-ion dynamics in molecules under intense laser pulses”, *J. Phys.: Condens. Matter*, **21**, 064222:1–5 (2009).
- ²³ M. R. Provorov and C. M. Isborn, “Electron dynamics with real-time time-dependent density functional theory”, *Int. J. Quantum Chem.*, **116**, 739–749 (2016).

- ²⁴ Y. Zhu and J. M. Herbert, “Self-consistent predictor/corrector algorithms for stable and efficient integration of the time-dependent Kohn-Sham equation”, *J. Chem. Phys.*, **148**, 044117:1–18 (2018).
- ²⁵ Y. Zhu, B. Alam, and J. M. Herbert, “Broadband x-ray absorption spectra from time-dependent Kohn-Sham calculations” (DOI: 10.26434/chemrxiv.14766960.v1).
- ²⁶ M. Lein and S. Kümmel, “Exact time-dependent exchange-correlation potentials for strong-field electron dynamics”, *Phys. Rev. Lett.*, **94**, 143003:1–4 (2005).
- ²⁷ X. Chu and P. J. Memoli, “Role of multiphoton excitation and two-electron effects in high harmonic generation of H₂: A TDDFT calculation”, *Chem. Phys.*, **391**, 83–87 (2011).
- ²⁸ X. Chu and G. C. Groenenboom, “Time-dependent density-functional-theory calculation of high-order-harmonic generation of H₂”, *Phys. Rev. A*, **85**, 053402:1–7 (2012).
- ²⁹ E. Luppi and M. Head-Gordon, “Computation of high-harmonic generation spectra of H₂ and N₂ in intense laser pulses using quantum chemistry methods and time-dependent density functional theory”, *Mol. Phys.*, **110**, 909–923 (2012).
- ³⁰ F. Bedurke, T. Klamroth, and P. Saalfrank, “Many-electron dynamics in laser-driven molecules: Wavefunction theory *vs.* density functional theory”, *Phys. Chem. Chem. Phys.*, **23**, 13544–13560 (2021).
- ³¹ S. Klinkusch, P. Saalfrank, and T. Klamroth, “Laser-induced electron dynamics including photoionization: A heuristic model within time-dependent configuration interaction theory”, *J. Chem. Phys.*, **131**, 114304:1–8 (2009).
- ³² A. F. White, C. J. Heide, P. Saalfrank, M. Head-Gordon, and E. Luppi, “Computation of high-harmonic generation spectra of the hydrogen molecule using time-dependent configuration-interaction”, *Mol. Phys.*, **114**, 947–956 (2016).
- ³³ C. F. Pauletti, E. Coccia, and E. Luppi, “Role of exchange and correlation in high-harmonic generation spectra of H₂, N₂, and CO₂: Real-time time-dependent electronic structure approaches”, *J. Chem. Phys.*, **154**, 014101:1–13 (2021).
- ³⁴ H. Iikura, T. Tsuneda, T. Yanai, and K. Hirao, “A long-range correction scheme for generalized-gradient-approximation exchange functionals”, *J. Chem. Phys.*, **115**, 3540–3544 (2001).
- ³⁵ M. A. Rohrdanz and J. M. Herbert, “Simultaneous benchmarking of ground- and excited-state properties with long-range-corrected density functional theory”, *J. Chem. Phys.*, **129**, 034107:1–9 (2008).
- ³⁶ A. W. Lange, M. A. Rohrdanz, and J. M. Herbert, “Charge-transfer excited states in a π -stacked adenine dimer, as predicted using long-range-corrected time-dependent density functional theory”, *J. Phys. Chem. B*, **112**, 6304–6308 (2008). Erratum: *J. Phys. Chem. B*, **112**, 7345 (2008).
- ³⁷ M. A. Rohrdanz, K. M. Martins, and J. M. Herbert, “A long-range-corrected density functional that performs well for both ground-state properties and time-dependent density functional theory excitation energies, including charge-transfer excited states”, *J. Chem. Phys.*, **130**, 054112:1–8 (2009).
- ³⁸ R. M. Richard and J. M. Herbert, “Time-dependent density-functional description of the ¹L_a state in polycyclic aromatic hydrocarbons: Charge-transfer character in disguise?”, *J. Chem. Theory Comput.*, **7**, 1296–1306 (2011).
- ³⁹ B. Alam, A. F. Morrison, and J. M. Herbert, “Charge separation and charge transfer in the low-lying excited states of pentacene”, *J. Phys. Chem. C*, **124**, 24653–24666 (2020).
- ⁴⁰ O. A. Vydrov, G. E. Scuseria, and J. P. Perdew, “Tests of functionals for systems with fractional electron number”, *J. Chem. Phys.*, **126**, 154109:1–9 (2007).
- ⁴¹ E. Luppi and M. Head-Gordon, “The role of Rydberg and continuum levels in computing high harmonic generation spectra of the hydrogen atom using time-dependent configuration interaction”, *J. Chem. Phys.*, **139**, 164121:1–9 (2013).
- ⁴² S. Ghimire, A. DiChiara, E. Sistrunk, P. Agostini, L. F. DiMauro, and D. Reis, “Observation of high-order harmonic generation in a bulk crystal”, *Nat. Phys.*, **7**, 138–141 (2011).
- ⁴³ T. T. Luu, Z. Yin, A. Jain, T. Gaumnitz, Y. Pertot, J. Ma, and H. J. Wörner, “Extreme-ultraviolet high-harmonic generation in liquids”, *Nat. Commun.*, **9**, 3723:1–10 (2018).
- ⁴⁴ A.-W. Zeng and X.-B. Bian, “Impact of statistical fluctuations on high harmonic generation in liquids”, *Phys. Rev. Lett.*, **124**, 203901:1–5 (2020).
- ⁴⁵ X. Chu and G. C. Groeneboom, “Contributions of inner-valence molecular orbitals and multiphoton resonances to high-order-harmonic generation of N₂: A time-dependent density-functional-theory study”, *Phys. Rev. A*, **93**, 013422:1–7 (2016).
- ⁴⁶ M. Lewenstein, P. Balcou, M. Y. Ivanov, A. L’Huillier, and P. B. Corkum, “Theory of high-harmonic generation by low-frequency laser fields”, *Phys. Rev. A*, **49**, 2117–2132 (1994).
- ⁴⁷ E. Coccia, R. Assaraf, E. Luppi, and J. Toulouse, “*Ab initio* lifetime correction to scattering states for time-dependent electronic-structure calculations with incomplete basis sets”, *J. Chem. Phys.*, **147**, 014106:1–9 (2017).
- ⁴⁸ T.-C. Jagau, K. B. Bravaya, and A. I. Krylov, “Extending the quantum chemistry of bound states to electronic resonances”, *Annu. Rev. Phys. Chem.*, **68**, 525–553 (2017).
- ⁴⁹ S. Klaiman and I. Gilary, “On resonance: A first glance in the behavior of unstable states”, *Adv. Quantum Chem.*, **63**, 1–31 (2012).
- ⁵⁰ J. M. Herbert, “The quantum chemistry of loosely-bound electrons”, in *Reviews in Computational Chemistry*, A. L. Parrill and K. Lipkowitz, Eds., Vol. 28; Wiley-VCH: Hoboken, NJ, 2015; chapter 8, pages 391–517.
- ⁵¹ U. V. Riss and H.-D. Meyer, “Investigation on the reflection and transmission properties of complex absorbing potentials”, *J. Chem. Phys.*, **105**, 1409–1419 (1996).
- ⁵² J. L. Krause, K. J. Schafer, and K. C. Kulander, “High-order harmonic generation from atoms and ions in the high intensity regime”, *Phys. Rev. Lett.*, **68**, 3535–3538 (1992).
- ⁵³ D.-S. Guo, C. Yu, J. Zhang, J. Gao, Z.-W. Sun, and Z. Sun, “On the cutoff law of laser induced high harmonic spectra”, *Front. Phys.*, **10**, 103201:1–6 (2015).
- ⁵⁴ E. K. U. Gross, C. A. Ullrich, and U. J. Gossmann, “Density functional theory of time-dependent systems”, in *Density Functional Theory*, E. K. U. Gross and R. M. Dreizler, Eds.; Plenum Press: New York, 1995; pages 149–171.
- ⁵⁵ C. Leforestier, R. H. Bisseling, C. Cerjan, M. D. Feit, R. Friesner, A. Guldberg, A. Hammerich, G. Jolicard, W. Karrlein, H.-D. Meyer, N. Lipkin, O. Roncero, and R. Kosloff, “A comparison of different propagation schemes for the time dependent Schrödinger equation”, *J. Comput. Phys.*, **94**, 59–80 (1991).
- ⁵⁶ X. Li, S. M. Smith, A. N. Markevitch, D. A. Romanov,

- R. J. Levis, and H. B. Schlegel, “A time-dependent Hartree–Fock approach for studying the electronic optical response of molecules in intense fields”, *Phys. Chem. Chem. Phys.*, **7**, 233–239 (2005).
- ⁵⁷ P. Krause and H. B. Schlegel, “Strong field ionization rates of linear polyenes simulated with time-dependent configuration interaction and an absorbing potential”, *J. Chem. Phys.*, **141**, 174104:1–7 (2014).
- ⁵⁸ P. Krause, J. A. Sonk, and H. B. Schlegel, “Strong field ionization rates simulated with time-dependent configuration interaction and an absorbing potential”, *J. Chem. Phys.*, **140**, 174113:1–7 (2014).
- ⁵⁹ P. Krause and H. B. Schlegel, “Angle-dependent ionization of small molecules by time-dependent configuration interaction and an absorbing potential”, *J. Phys. Chem. Lett.*, **6**, 2140–2146 (2015).
- ⁶⁰ P. Hoerner and H. B. Schlegel, “Angular dependence of strong field ionization of CH_3X ($\text{X} = \text{F}, \text{Cl}, \text{Br}, \text{or I}$) using time-dependent configuration interaction with an absorbing potential”, *J. Phys. Chem. A*, **121**, 5940–5946 (2017).
- ⁶¹ P. Hoerner, W. Li, and H. B. Schlegel, “Sequential double ionization of molecules by strong laser fields simulated with time-dependent configuration interaction”, *J. Chem. Phys.*, **155**, 114103:1–8 (2021).
- ⁶² S. Dasgupta and J. M. Herbert, “Standard grids for high-precision integration of modern density functionals: SG-2 and SG-3”, *J. Comput. Chem.*, **38**, 869–882 (2017).
- ⁶³ E. Epifanovsky, A. T. B. Gilbert, X. Feng, J. Lee, Y. Mao, N. Mardirossian, P. Pokhilko, A. F. White, M. P. Coons, A. L. Dempwolff, Z. Gan, D. Hait, P. R. Horn, L. D. Jacobson, I. Kaliman, J. Kussmann, A. W. Lange, K. U. Lao, D. S. Levine, J. Liu, S. C. McKenzie, A. F. Morrison, K. D. Nanda, F. Plasser, D. R. Rehn, M. L. Vidal, Z.-Q. You, Y. Zhu, B. Alam, B. J. Albrecht, A. Aldossary, E. Alguire, J. H. Andersen, V. Athavale, D. Barton, K. Begam, A. Behn, N. Bellonzi, Y. A. Bernard, E. J. Berquist, H. G. A. Burton, A. Carreras, K. Carter-Fenk, R. Chakraborty, A. D. Chien, K. D. Closser, V. Cofer-Shabica, S. Dasgupta, M. de Wergifosse, J. Deng, M. Diedenhofen, H. Do, S. Ehlert, P.-T. Fang, S. Fatehi, Q. Feng, T. Friedhoff, J. Gayvert, Q. Ge, G. Gidofalvi, M. Goldey, J. Gomes, C. E. González-Espinoza, S. Gulania, A. O. Gunina, M. W. D. Hanson-Heine, P. H. P. Harbach, A. Hauser, M. F. Herbst, M. Hernández Vera, M. Hodecker, Z. C. Holden, S. Houck, X. Huang, K. Hui, B. C. Huynh, M. Ivanov, A. Jász, H. Ji, H. Jiang, B. Kaduk, S. Kähler, K. Khistyayev, J. Kim, G. Kis, P. Klunzinger, Z. Koczor-Benda, J. H. Koh, D. Kosenkov, L. Koulias, T. Kowalczyk, C. M. Krauter, K. Kue, A. Kunitsa, T. Kus, I. Ladjánszki, A. Landau, K. V. Lawler, D. Lefrancois, S. Lehtola, R. R. Li, Y.-P. Li, J. Liang, M. Liebenthal, H.-H. Lin, Y.-S. Lin, F. Liu, K.-Y. Liu, M. Loipersberger, A. Luenser, A. Manjanath, P. Manohar, E. Mansoor, S. F. Manzer, S.-P. Mao, A. V. Marenich, T. Markovich, S. Mason, S. A. Maurer, P. F. McLaughlin, M. F. S. J. Menger, J.-M. Mewes, S. A. Mewes, P. Morgante, J. W. Mullinax, K. J. Oosterbaan, G. Parani, A. C. Paul, S. K. Paul, F. Pavošević, Z. Pei, S. Prager, E. I. Proynov, A. Rák, E. Ramos-Cordoba, B. Rana, A. E. Rask, A. Rettig, R. M. Richard, F. Rob, E. Rossomme, T. Scheele, M. Scheurer, M. Schneider, N. Sergueev, S. M. Sharada, W. Skomorowski, D. W. Small, C. J. Stein, Y.-C. Su, E. J. Sundstrom, Z. Tao, J. Thirman, G. J. Tornai, T. Tsuchimochi, N. M. Tubman, S. P. Veccham, O. Vydrov, J. Wenzel, J. Witte, A. Yamada, K. Yao, S. Yeganeh, S. R. Yost, A. Zech, I. Y. Zhang, X. Zhang, Y. Zhang, D. Zuev, A. Aspuru-Guzik, A. T. Bell, N. A. Besley, K. B. Bravaya, B. R. Brooks, D. Casanova, J.-D. Chai, S. Coriani, C. J. Cramer, G. Cserey, A. E. DePrince III, R. A. DiStasio Jr., A. Dreuw, B. D. Dunietz, T. R. Furlani, W. A. Goddard III, S. Hammes-Schiffer, T. Head-Gordon, W. J. Hehre, C.-P. Hsu, T.-C. Jagau, Y. Jung, A. Klamt, J. Kong, D. S. Lambrecht, W. Liang, N. J. Mayhall, C. W. McCurdy, J. B. Neaton, C. Ochsenfeld, J. A. Parkhill, R. Peverati, V. A. Rassolov, Y. Shao, L. V. Slipchenko, T. Stauch, R. P. Steele, J. E. Subotnik, A. J. W. Thom, A. Tkatchenko, D. G. Truhlar, T. Van Voorhis, T. A. Wesolowski, H. L. W. K. B. Whaley, P. M. Zimmerman, S. Faraji, P. M. W. Gill, M. Head-Gordon, J. M. Herbert, and A. I. Krylov, “Software for the frontiers of quantum chemistry: An overview of developments in the Q-Chem 5 package”, *J. Chem. Phys.*, **155**, 084801:1–59 (2021).
- ⁶⁴ T. S. Nguyen and J. Parkhill, “Nonadiabatic dynamics for electrons at second-order: Real-time TDDFT and OSCF2”, *J. Chem. Theory Comput.*, **11**, 2918–2924 (2015).
- ⁶⁵ T. S. Nguyen, J. H. Koh, S. Lefelhocz, and J. Parkhill, “Black-box, real-time simulations of transient absorption spectroscopy”, *J. Phys. Chem. Lett.*, **7**, 1590–1595 (2016).
- ⁶⁶ C. Witzorky, G. Paramonov, F. Bouakline, R. Jaquet, P. Saalfrank, and T. Klamroth, “Gaussian-type orbital calculations for high harmonic generation in vibrating molecules: Benchmarks for H_2^+ ”, *J. Chem. Theory Comput.* (DOI: 10.1021/acs.jctc.1c00837).
- ⁶⁷ D. E. Woon and T. H. Dunning Jr., “Gaussian basis sets for use in correlated molecular calculations. IV. Calculation of static electrical response properties”, *J. Chem. Phys.*, **100**, 2975–2988 (1994).
- ⁶⁸ F. Bedurke, T. Klamroth, P. Krause, and P. Saalfrank, “Discriminating organic isomers by high harmonic generation: A time-dependent configuration interaction singles study”, *J. Chem. Phys.*, **150**, 234114:1–10 (2019).
- ⁶⁹ X. Li, N. Govind, C. Isborn, A. E. DePrince III, and K. Lopata, “Real-time time-dependent electronic structure theory”, *Chem. Rev.*, **120**, 9951–9993 (2020).
- ⁷⁰ Ohio Supercomputer Center, <http://osc.edu/ark:/19495/f5s1ph73>.